Exchange-mediated reduction of magnetocrystalline anisotropy in textured Co-Pt nanowire arrays

Angelo Villegas[1,2], Martina Arce[1,2], Fernando Meneses[1], Silvia E. Urreta[1], Paula G. Bercoff[1,2,*]

[1] Universidad Nacional de Córdoba. Facultad de Matemática, Astronomía, Física y Computación (FAMAF). Ciudad Universitaria, 5000 Córdoba, Argentina.
[2] CONICET, Instituto de Física Enrique Gaviola (IFEG). Ciudad Universitaria, 5000 Córdoba, Argentina.

*Corresponding author: Paula G. Bercoff. paula.bercoff@unc.edu.ar . Tel: +54 351 53 53 701 (ext. 41269)

Abstract

The magnetocrystalline contribution to the effective anisotropy in arrays of electrodeposited Co and $Co_{90}Pt_{10}$ nanowires is investigated as a function of crystallographic texture, grain size, and inter-wire interactions. The nanowires are polycrystalline, with hcp grains exhibiting a strong texture in which the crystallographic c-axis lies predominantly perpendicular to the wire axis.

Within a conventional uniaxial anisotropy framework, the effective anisotropy is typically described as the balance between shape, dipolar interaction, and magnetocrystalline contributions. However, we show that this approach fails to quantitatively account for the magnetic behavior of Co-Pt nanowire arrays. In particular, the predicted easy axis orientation and anisotropy magnitude are inconsistent with the angular dependence of the hysteresis loops. This discrepancy is attributed to the combined effects of strong crystallographic texture and reduced grain size. In Co-Pt nanowires, grain sizes (10-18 nm) approach the exchange length, leading to significant inter-grain exchange coupling and an effective reduction of the magnetocrystalline anisotropy. As a result, the intrinsic anisotropy is no longer well described by bulk values but instead reflects an exchange-averaged anisotropy landscape.

By varying the template porosity, the relative importance of dipolar inter-wire interactions is tuned. In high-porosity arrays, magnetostatic interactions dominate the reversal process, whereas in low-porosity arrays with smaller grains, exchange interactions within individual nanowires play a key role. These conclusions are supported by first-order reversal curve (FORC) analysis, which reveals distinct interaction regimes through differences in coercive and interaction field distributions.

Keywords: Co-rich Co-Pt nanowire arrays; electrodeposition; crystallographic texture; exchange coupling; dipolar inter-wire interaction; effective magnetocrystalline anisotropy.

1. Introduction

Co nanowires (NWs) [1] are relatively strong ferromagnets with a Curie temperature of about 1400 K, and many technological applications such as in the rare-earth free magnets industry [2,3], in biomedical interventions [4,5], and as magnetic sensors and detectors [6]. Alloyed with noble metals Co NWs are key pieces for many applications in electrochemistry and catalysis [7-10].

It is well known that depending on composition, template geometry and processing route, electrodeposited Co and Co-rich NWs may exhibit quite different microstructures. Individual NWs may be biphasic, with a mix of *hcp* and *fcc* Co or Co-rich grains, or monophasic (pure Co or a solid solution) with *hcp* grains oriented in particular directions relative to the NW axis, leading to a strong crystallographic texture [11]. The microstructure of individual NWs in the array is found to depend on the processing variables such as the deposition mode (dc/ac mode) [12], the electrodeposition voltage [13], the metal ion concentration in the feeding solution [14] and the electrolyte pH [15,16].

The hard magnetic properties of these NWs are reported to be strongly dependent on the NW microstructure, shape, size and on the intrinsic magnetocrystalline anisotropy of the material. In addition, when NWs are

assembled into an array (as in anodized aluminum oxide hexagonally ordered templates) or forming more complex devices, dipolar interactions between them may largely affect the magnetic performance of the ensemble. This multivariable magnetic response, is commonly analyzed by considering a single, uniaxial effective magnetic anisotropy energy density K_{eff} (with an apparent easy axis parallel or perpendicular to the NWs axis) resulting from the interplay of the different energy density contributions from each nanowire and the inter-wire interaction term in the array [17-21].

In Co-based NW arrays, this effective uniaxial anisotropy constant K_{eff} is often approximated by the algebraic sum of positive (magnetizing, anisotropy field parallel to the NW axis) and negative (demagnetizing, anisotropy field on the array plane) energy terms [21]. These terms arise from three main contributions: the magnetostatic shape anisotropy energy, K_{SH}, of each nanowire (NW) in the array, the inter-wire dipolar interaction within the array, K_{int}, and the magnetocrystalline anisotropy energy K_{MC} of each NW. The individual easy axis directions corresponding to these three contributions are not collinear and in some cases they are perpendicular. In principle, K_{MC} is expected to depend on the crystalline phases present in the NWs, their composition and spatial distribution, as well as microstructural features such as grain or phase size, defects, and crystallographic texture. Notably, when modeling the magnetocrystalline contribution to the effective uniaxial anisotropy, these internal microstructural parameters are often disregarded. In particular, it is not clear how eventual multiple easy/hard magnetocrystalline axes in each NW are reduced to a unique uniaxial K_{MC} value.

In this work we shortly discuss the *apparent* magnetocrystalline contribution K_{MC} to the effective anisotropy K_{eff} in a uniaxial anisotropy model for polycrystalline, monophasic Co-based NW arrays exhibiting different crystallographic texture, grain size and composition. It is found that Pt addition reduces the grain size and increases the crystallographic texture of individual NWs, compared to those detected in pure Co. These changes are shown to influence the effective anisotropy constant K_{eff} of the array –its magnitude and the direction of the corresponding easy/hard axis– leading to more complex collective magnetic behaviors. It is found that texture may tilt the collective easy axis of the array to produce an easy plane, strongly competing with the shape anisotropy term. In addition, the influence of inter-wire dipolar interactions on the effective anisotropy is explored by changing the template porosity. In this case, the effective anisotropy energy and the easy axis direction predicted by the model are not consistent with the angular dependence of the hysteresis loops parameters.

2. Experimental procedures

Anodic Aluminum Oxide (AAO) templates were prepared following the well-known two-step anodization method described in [21]. Shortly, highly pure Al foils (99.997%) were first electropolished and then anodized at 40 V for 24 h in 0.3 M oxalic acid. This first anodization was removed and subsequently a second anodizing step of 20 h was carried out under the same conditions of the first. Then, the remaining aluminum was dissolved and the pores were opened in a 5% v/v H_3PO_4 solution. After this, a thin gold layer was sputtered to serve as electric contact. The so-obtained templates have $D_P = (55 \pm 5)$ nm diameter pores and $d_{cc} = (115 \pm 10)$ nm center-to-center pore distance. Considering a hexagonal packing arrangement, the porosity can be calculated as $P = \pi/2\sqrt{3(D_P/d_{cc})}$ [22], giving 22%. The NW prepared with these templates replicate cylinders of 55 nm diameter.

Also, the hard anodization technique [23] was used to obtain alumina templates with 140 nm diameter pores and *P*=29%. Briefly, a high-purity aluminum foil was submitted under galvanostatic–potentiostatic conditions in an acidic electrolyte. To ensure a controlled transition to the high-field regime and to prevent dielectric breakdown, the anodization voltage was increased linearly at a rate of 5.6 V·min^{-1} until reaching a maximum value of 130 V, at a constant temperature of 2 ºC. This gradual voltage ramp enables stable oxide growth by limiting Joule heating and mechanical stress within the forming layer. Once the target voltage was attained, the anodization proceeded under constant voltage for additional 40 min to promote the formation of straight, vertically aligned pores with high aspect ratio. The resulting pore diameter and interpore distance are governed by the applied voltage, yielding well-defined and homogeneous templates. We obtained templates with mean pore diameter of (140 ± 5) nm and mean center-to-center distance of (100 ± 20) nm.

Electrodeposition of Co NWs was performed in a three electrode cell, from a feeding solution containing 0.3 M $CoSO_4$ and 0.3 M H_3BO_3 at pH = 3. CoPt NWs were electrodeposited in the same conditions as those described in [21] for the sample of composition $Co_{90}Pt_{10}$. Crystalline phases in the NWs arrays were determined using X-ray diffraction (XRD) on a PANalytical PW3830 diffractometer, using Cu Kα radiation (λ = 0.15418 nm) in the Bragg-Brentano configuration. The NWs morphology was studied using a Sigma Zeiss Field Emission Scanning Electron Microscope (FE-SEM), with an attached Oxford Energy Dispersive Spectrometer (EDS) which allowed determining the chemical composition.

$M(H)$ curves were measured at room temperature in a VSM Lakeshore 7300 magnetometer, with maximum applied fields of ±1.8 T, which allowed to saturate the samples. Hysteresis loops were recorded at different angles between the NW axis direction and the applied field, from $\varphi = 0^o$ (PA: parallel configuration) to $\varphi = 90^o$ (PE: perpendicular configuration). Before each angular measurement, the centering of the sample was controlled, following the usual VSM protocol. First order reversal curves (FORCs) were also measured both in PA and PE configurations.

The prepared samples are named according to their nominal composition and the corresponding NW diameter as Co55 for pure cobalt and CoPt55 for the nominal $Co_{90}Pt_{10}$ alloys with NW diameter of 55 nm, while CoPt140 represents the sample of $Co_{90}Pt_{10}$ nominal composition and 140 nm wire diameter.

3. Results and Discussion

3.1 Microstructure

Figures 1a and 1c illustrate typical views of Co55 and CoPt140 NWs, respectively, after complete dissolution of the alumina template. Figure 1b displays a lateral view of CoPt55 with the NWs inside the tubular alumina pores and a close-up view in the inset. The morphology of the electrodeposited NWs is quite uniform; the resulting NWs geometric parameters are given in Table 1.

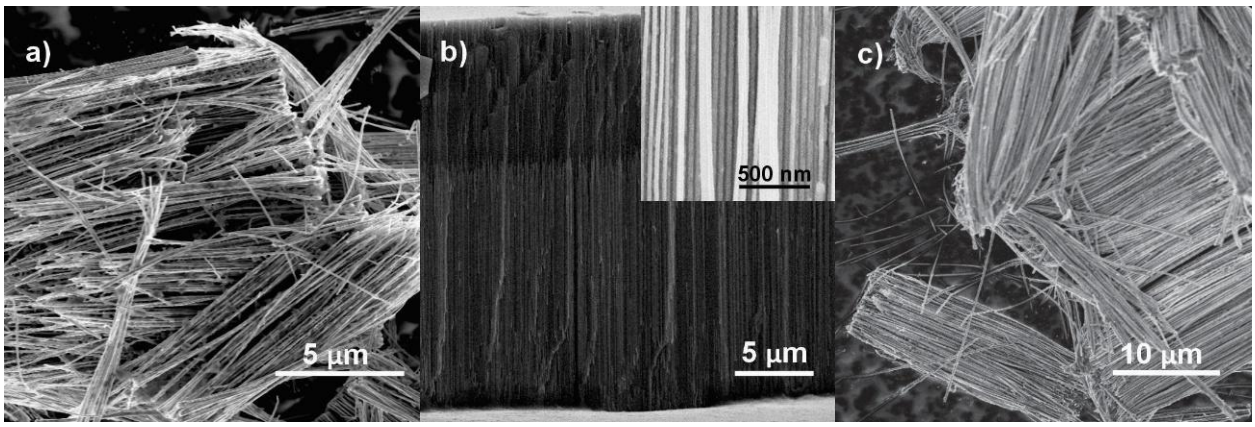

Figure 1. SEM images of a) Co55, b) CoPt55 and c) CoPt140 NWs. The inset in b) displays a lateral view of CoPt55 NWs inside the alumina template.

The alloy composition was determined by EDS, after measuring extended areas of different samples in the as-deposited condition, to obtain a mean value of Co (90±5) at. % for CoPt55 and Co (93±5) at. % for CoPt140 NW arrays. The crystalline phases in the different samples were investigated by XRD in the as-deposited condition (Figure 2a), keeping the wires inside the pores of the template.

Table 1. Main parameters of the arrays: template nominal porosity *P*, mean NW diameter *d*, and length *L*. The mean crystallite size d_S, estimated using the Scherrer formula, the corresponding Harris texture T_{hkl} coefficient and the fraction of each crystal orientation *f* are also listed.

Sample	*P* [%]	*d* [nm]	*L* [μm]	d_S [nm]	T_{hkl}	*f* [%]
Co55	22	55 ± 5	8.5±0.5	47± 5	(100) 0.9 (110) 2.1 (002) ~ 0	30.6% 69.2% 0.2%
CoPt55	22	55 ± 5	16.0 ±0.5	10 ± 5	(100) 1.6 (101) 0.4	80% 20%
CoPt140	29	140 ± 10	26.0 ±0.5	18 ± 5	(100) 1.8 (101) 0.2	92% 8%

The Harris texture coefficient *T*(*hkl)* in the ordered arrays was estimated by considering the *hcp* (100), (110) and (002) reflections for Co sample, while the (100), (110) and the (101) peaks were used for CoPt arrays. *T*(*hkl)* was determined following the well-known expression [24]:

$$T\ (hkl)_i = \frac{I(hkl)_i / I_0(hkl)_i}{\frac{1}{N}\sum I(hkl)_n\ / I_0(hkl)_n}$$

were *hkl* are the Miller indices, $(hkl)_i$ is the observed intensity of the (*hkl*) plane, $I_0(hkl)_n$ is the standard intensity of the reflected plane, and *N* is total number of reflected planes that are considered for the calculation. For each sample, the percentage of each crystallographic texture in the array relative to the total $\sum \frac{I(hkl)}{I_0(hkl)}$ is shown as a pie graph in the corresponding pattern of Figure 2a. Geometric aspects of the process are schematized in Figure 2b. The peaks marked with open triangles in the diffractogram of Co55 corresponds to gold remains, sputtered for electrical contact. Reflections corresponding to the SiO_2 sample holder are identified in the CoPt55 pattern with open circle. The Scherrer crystallite size d_S [25], and the texture index obtained for the three samples, are listed in Table 1.

Sample Co55 crystallizes in a *hcp*-Co structure, in agreement with file PDF 96-901-1616, with a marked crystallographic texture along the (110) and (100) directions. The diffractograms of Co-Pt NWs indicate that in both cases they consist of a disordered solid solution *hcp* Co(Pt) phase (COD-9008492). CoPt55 and CoPt140 exhibit a contribution of the (101) reflection, which indicates that a volume fraction of the grains have the hexagonal c-axis oriented at φ=62° from the NW axis.

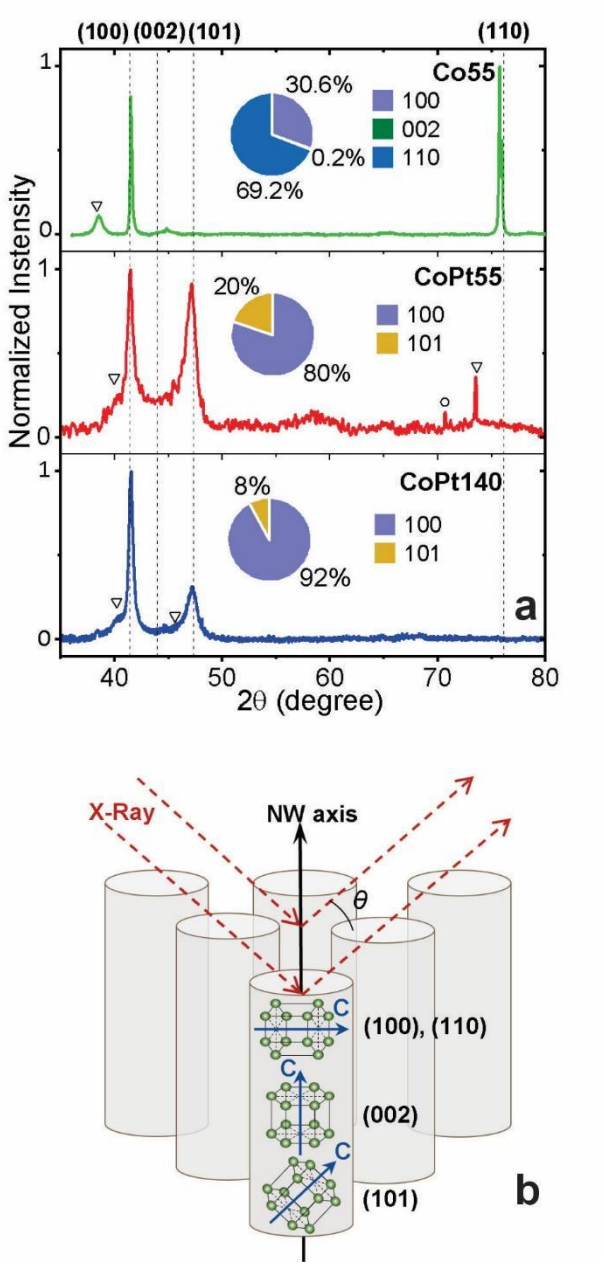

Figure 2. a) XRD patterns corresponding to samples Co55, CoPt55 and CoPt140, together with the resulting volume fraction of the crystallographic orientations in each array. Dashed vertical lines indicate the positions of Co *hcp* reflections. The peaks indexed with open triangles correspond to remains of sputtered gold and the one indexed with open circle come from the SiO_2 sample holder. b) Scheme illustrating that the NWs are polycrystalline with a relatively large (100)/(110) crystallographic texture. The pie plots inserted in a) indicate the respective volume fraction of grains in the array with a given orientation, relative to the NW axis.

Summarizing, the NWs in the three arrays are single-phase, polycrystalline systems, with small *hcp* grains mainly oriented with their "c" axis perpendicular to the wire length.

3.2 Effective magnetic anisotropy of the nanowire array

As stated before, all the NWs are formed by small, textured grains of the *hcp*-Co or *hcp*-CoPt phase (see Table I). In the uniaxial anisotropy approach, the effective anisotropy energy density in a given array may be described as [21]:

$$K_{eff} = K_{SH} - K_{int} - K_{MC} \quad (1)$$

being K_{SH} the shape anisotropy of the individual cylindrical NWs (positive, favoring magnetization along the wire axis), K_{int} the anisotropy arising from the dipolar interaction between individual wires in the ensemble (negative, favoring orientation normal to the wire axis, on the array's plane) and K_{MC} the magnetocrystalline anisotropy of the NWs, assumed negative in our samples, as texture favors an easy axis for this contribution which is normal to the wires longitudinal axis.

The magnitude of the magnetostatic shape energy associated to individual cylindrical NWs may be approximated by the expression $K_{SH} \cong \frac{1}{2} \Delta N \mu_0 M_S^2$ [21], where ΔN is difference between the demagnetizing factors parallel and perpendicular to the NW´s axis and μ_0 is the vacuum magnetic permittivity. Because of the large aspect ratios in all the arrays, a value $\Delta N \cong 1/2$ is adopted.

The dipolar interaction energy constant was estimated following the approach proposed by Fatih Zighem et *al.* [26], using $K_{int} = \frac{1}{2} \pi \mu_0 M_S^2 P^*$, where P^* = 0.9 P represents an effective porosity considering a template filling factor of ~90%. It should be noted that this expression constitutes a mean-field approximation that assumes a spatially uniform magnetization and neglects local dipolar field fluctuations and positional disorder within the array. Consequently, it is strictly valid only for uniformly magnetized states (e.g., near saturation) and may not accurately describe the system during magnetization reversal, where non-uniform configurations such as domain wall propagation or curling modes can occur. In addition, the model assumes infinitely long cylindrical nanowires and does not account for finite-size effects or deviations from ideal geometry. The use of an effective filling factor P^* introduces further uncertainty, as it empirically accounts for structural template imperfections. Therefore, the estimated K_{int} should be regarded as an upper-bound approximation of the dipolar interaction strength, particularly in arrays with larger diameters or enhanced magnetic non-uniformity. Being of magnetostatic origin, K_{SH} and K_{int} embody the main demagnetizing effects in the array; extra contributions from the diamagnetic alumina template are ignored.

A quantitative description of the *apparent* magnetocrystalline energy K_{MC} must consider that cylindrical NWs are polycrystalline, with relatively small (10-50 nm) *hcp* grains, so each nanowire has a magnetocrystalline anisotropy (strength and easy/hard axis orientations) involving the weighted average of these vectorial magnitudes inside the individual grains. The crystallographic texture detected in XRD patterns (Figure 2a) indicates that in all samples most of the grains have the crystallographic hexagonal *c* axis pointing normally to the NWs' axis, to the (100) and (110) orientations, with almost no grains having the *c* axis parallel to the NW´s axis (~ 0.2 % in sample Co55 and 0% in both alloy arrays) –see Figure 2b. Only sample CoPt55, containing 20% of its volume with grains in an intermediate orientation, may cooperate to a certain extent with shape anisotropy, an effect that is lessened by the quite small grain size in the array (~10 nm). Then, the crystallographic easy axes of the majority grains may be considered as uniformly distributed on the plane of the array (as in an easy plane configuration), assuming an azimuthal symmetry in the distribution, as also proposed for the demagnetizing field arising from the dipolar interaction between NWs in the array. Then, as a first approximation it may be considered $K_{MC} = K_U$, being $K_U = K_1 + K_2$ with K_1 and K_2 the first and second anisotropy constants of *hcp*-Co, at 300 K. K_U is then a uniaxial magnetocrystalline anisotropy constant.

A unique value of uniaxial crystalline anisotropy is used for Co and CoPt alloys. Even when Co–Pt hybridization and the large spin–orbit coupling of Pt can contribute to magnetic anisotropy, this is mainly observed in Pt/Co multilayers and ultrathin films where chemically sharp interfaces appear. However, in our alloyed samples where disordered solid solutions crystallize, no such features are present, thereby allowing us to disregard this contribution to the effective anisotropy of the arrays.

The effective anisotropy and the corresponding easy axis can be then estimated for the three samples. The different anisotropy terms under consideration in Eq. (1), estimated using the parameters indicated above, are listed in Table 2.

The values of K_{eff} resulting from Eq. (1) are all negative, predicting that in the three arrays the collective easy axis is tilted towards the plane normal to the NW longitudinal axis, as a result of the overcompensation of the shape contribution. As it will be shown in the next section, these predictions are not consistent with the angular trends of coercivity and remanence in CoPt55 and CoPt140 arrays.

3.3 Magnetic hysteresis

Measurements of the angular dependence of the hysteresis loops for all the arrays were performed to further explore the characteristics of the effective magnetic anisotropy in each case. The angular dependence of the relative remanence provides information on the orientation and distribution of the effective easy axis, while the angular dependence of the coercivity also reflects the underlying magnetization reversal mechanism. A strong angular variation of this later parameter indicates a well-defined anisotropy and largely independent switching, whereas a flattened dependence reveals the increasing role of dipolar interactions and collective reversal processes within the array. The hysteresis loops were measured at different relative orientations φ of the applied magnetic field and the NW axis, in the range -90º ≤ φ ≤ 90º.

Table 2. Magnetic parameters in the uniaxial effective anisotropy model. Anisotropy energy associated to shape (K_{SH}) and interaction (K_{int}) magnetostatic effects, $K_U = K_1 + K_2$ the magnetocrystalline constants in array. The value of K_{eff} resulting from the balance in Eq. (1) and the effective anisotropy constant K_{eff}^{area}, independently determined using the area method, are also listed. Values of the magnetocrystalline constant $K_U^{\star}$ satisfying Eq. (1) for K_{eff}^{area}, the factor α defined by $K_U^{\star} = \alpha K_U$, and the extent of grain volume affected by exchange interaction, V_{exch} are also listed for each array.

	Co55	**CoPt55**	**CoPt140**
$\mu_0 M_s \pm 0.1$ [T]	1.8	1.6	1.6
$K_U \pm 0.1$ [10^5 J m^{-3}]	5.1	5.1	5.1
P (P^*)	0.22 (0.20)	0.22 (0.20)	0.29 (0.26)
$K_{SH} \pm 0.01$ [10^5 J m^{-3}]	6.37	5.16	5.16
$K_{int} \pm 0.01$ [10^5 J m^{-3}]	2.54	2.00	2.64
-($K_{int} + K_U$)[10^5 J m^{-3}]	7.64	7.10	7.74
$K_{eff} \pm 0.01$ [10^5 J m^{-3}]	-1.27	-1.94	-2.58
K_{eff}^{area} [10^5 J m^{-3}]	0.11	1.19	0.25
$K_U^{\star}$ [10^5 J m^{-3}]	3.72	1.99	2.27
α	0.73	0.39	0.45
V_{exch} [%]	18	90	60

The curves corresponding to φ = 0° (field parallel to the NW axis, denoted PA) and φ = ±90° (perpendicular, denoted PE) are shown in Figure 3. In this figure, the room temperature hysteresis loops of the arrays Co55 (Figure 3a) and CoPt55 (Figure 3b), with identical templates but different compositions, are displayed, together with those of CoPt140 (Figure 3c) with the same composition than CoPt55 but larger template porosity.

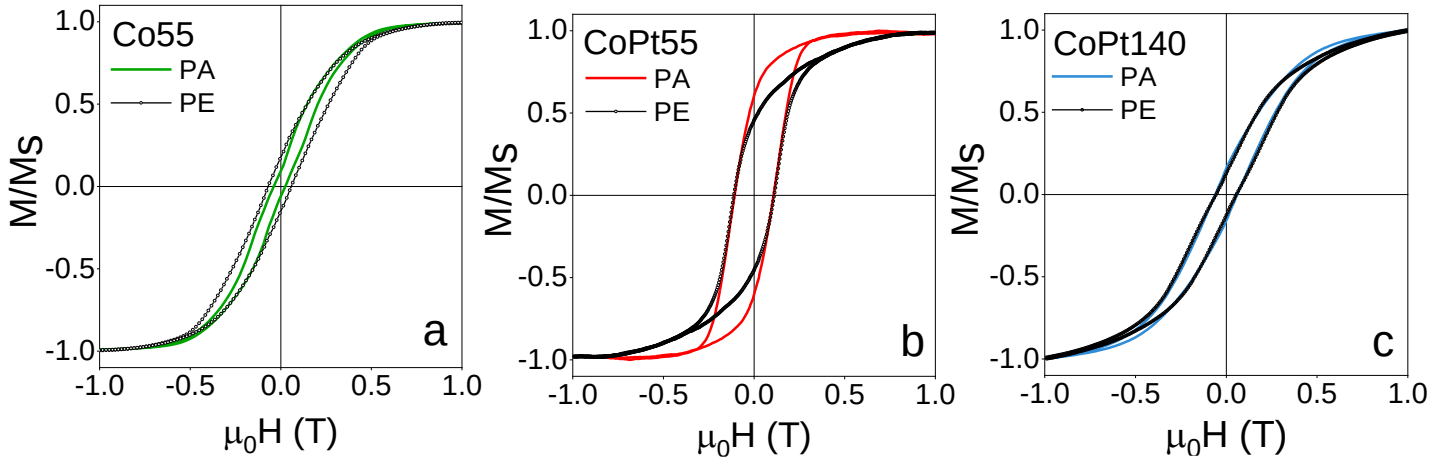

Figure 3. Normalized room temperature hysteresis loops with the magnetic field applied in both PA and PE orientations, of arrays (a) Co55, (b) CoPt55 and (c) CoPt140. The loops were measured with maximum applied fields of ±1.8 T, but a ±1.0 T range is shown, for clarity.

The hysteresis loop of array Co55 is characteristic of competing, comparable anisotropies leading to a relatively small effective anisotropy, and in this case there is an easy (plane) normal to the NW axis. This is confirmed by the angular dependence of the coercive field $\mu_0 H_C$ and the relative remanence S ($=M_R/M_S$) shown in Figure 4, where both magnitudes have a maximum in the PE orientation (±90°), indicating that this is the easy axis direction (easy plane). Magnetocrystalline anisotropy reinforces the demagnetizing effect of dipolar inter-wire interactions and together compensate the shape anisotropy, tilting the collective easy axis.

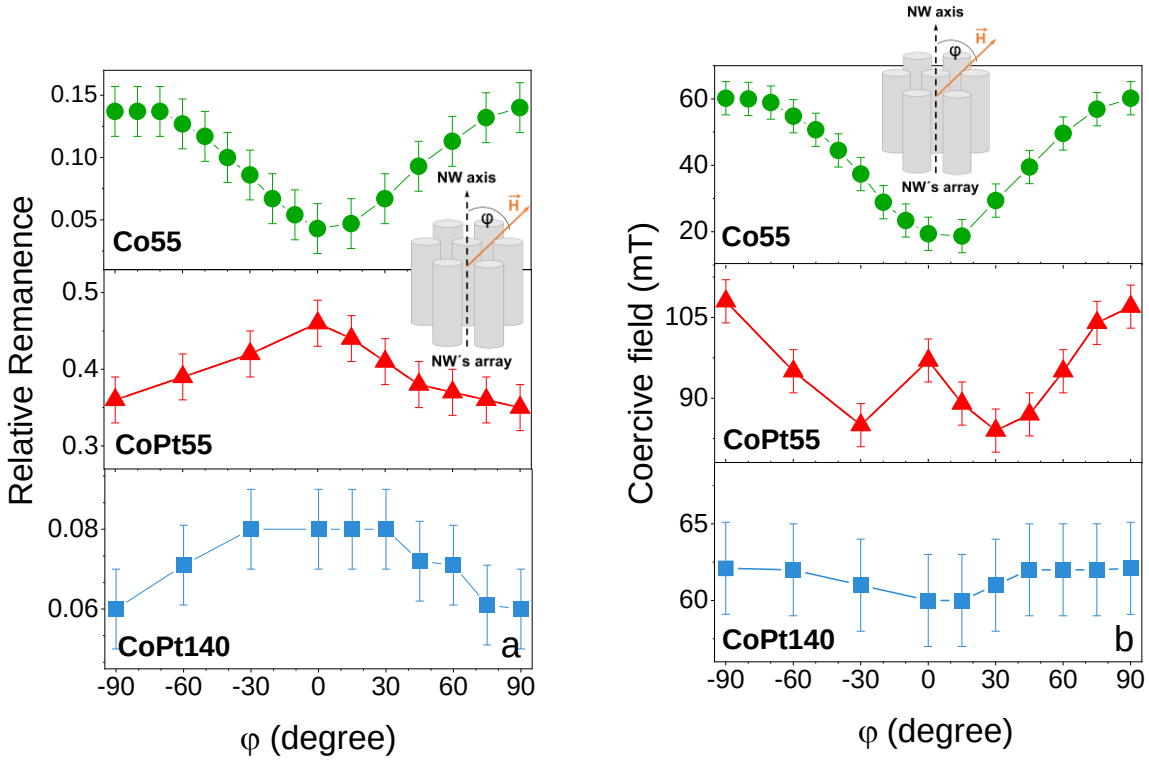

Figure 4. Room temperature angular dependence of (a) the relative remanence S, and (b) the coercive field $\mu_o H_C$ for the studied arrays.

In other words, the observed angular dependence of the coercive field in Co55 is consistent with the collective easy axis predicted by the minimum free energy approach, assuming an in-plane magnetocrystalline anisotropy competing with shape and assisted by dipolar inter-wire interactions. The angular evolution of the relative remanence is similar, supporting this interpretation. Co55 represents a regime in which the effective magnetic easy axis is tilted 90° relative to the nanowire axis (in plane). Concerning the strong variation of H_c in this sample, it likely results from a unique mechanism acting in the complete angular range, without any transition to another one at intermediate angles, as indicated by the smooth variations of both, H_c and S.

On the other hand, the PA and PE hysteresis loops of array CoPt55 display a more complex angular behavior consistent with an easy axis closer to the wires axis, likely due to the cooperative contribution of the 20% volume fraction of grains oriented with the (101) texture. This enhanced magnetocrystalline anisotropy with respect to Co55 competes with the demagnetizing magnetostatic interactions. In fact, a clear easy axis as governed by shape anisotropy is observed in the PA direction. This is further confirmed by the angular dependence of the relative remanence in this array shown in Figure 4a. It exhibits a clear maximum at φ = 0° and smoothly decreases to the minima at φ ±90°. The coercive field behavior in this array is more complex, as seen in Figure 4b. It also has a local maximum at the PA direction but it behaves non monotonically towards the PE direction, going through local minima near φ = ±30°. This non-monotonic behavior of CoPt55 is better attributed to nucleation and pinning processes in a heterogeneous anisotropy landscape. The occurrence of coercivity minima near φ = ±30° suggests that magnetization reversal is most efficiently activated at intermediate field orientations. This behavior is consistent with a non-coherent, nucleation-controlled reversal process arising from the competition between wire-shape anisotropy, reduced but non-negligible in-plane magnetocrystalline anisotropy, and dipolar interactions. Under these conditions, the minimum switching field does not necessarily coincide with the principal easy axis, but rather with the direction that minimizes the nucleation barrier.

The hysteresis loops of the array CoPt140 for the two orientations shown in Figure 3c for the two orientations are practically indistinguishable, indicating a quite small effective anisotropy and a strong competition between different anisotropies. In this scenario, the contribution from the 8% of the (101) texture is not enough to overcome the quite strong demagnetizing magnetostatic effects. The approach described by Eq. (1) predicts a collective easy axis at φ = 90° (along the PE direction) but a clear easy axis could not be determined within experimental errors. This is evidenced by the angular dependence of the relative remanence and the coercive field displayed in Figure 4, which is larger at small angles but shows a flat, quite isotropic behavior. In contrast, the nearly angle-independent coercivity of CoPt140 indicates that dipolar interactions dominate the reversal process, leading to collective switching and a suppression of the effective anisotropy contrast.

The failure of the uniaxial anisotropy model to describe the Co-Pt nanowire arrays indicates that the assumption of a single effective magnetocrystalline anisotropy term is not valid in these systems. Although the model captures the qualitative competition between shape and dipolar contributions, it neglects the complex internal structure of the nanowires.

In particular, the combination of strong crystallographic texture and reduced grain size leads to a distribution of local anisotropy axes within each nanowire. When the grain size approaches the exchange length, inter-grain exchange coupling promotes a partial averaging of these anisotropies. As a result, the effective magnetocrystalline contribution is significantly reduced compared to the bulk anisotropy constant and cannot be represented by a simple scalar term.

This exchange-mediated reduction explains why the experimentally observed easy axis remains aligned with the nanowire axis in Co-Pt samples, despite the in-plane orientation of the crystallographic easy axes.

To perform an estimation of the magnitude of the actual magnetocrystalline anisotropy K_U^* acting in these arrays, the effective anisotropy K_{eff}^{area} of the three arrays was independently estimated from the hysteresis loops in Figure 3, by applying the well-known area method that calculates the difference of the PA and PE loops areas [27]; the resulting values are listed in Table 2. It should be noted that deviations from the Stoner-Wohlfarth conditions limit the applicability of the area method for determining K_{eff} and that it is less accurate when the parallel (PA) and perpendicular (PE) hysteresis loops are similar. Introducing this value of effective

anisotropy in Eq. (1), the apparent magnetocrystalline anisotropies K_U^* contributing to the collective behavior can be estimated. They are $K_U^* = \alpha\ K_U$, all smaller than the ones originally considered, by a factor $\alpha < 1$. The resulting values of K_U^* and α are included in Table 2. Despite the factor α lacks predictive capability, it is a phenomenological indicator of non-ideality within the effective magnetocrystalline anisotropy energy, a concept previously established for nanostructured magnetic materials and composites with nanometric grain sizes [28].

It may be observed that the anisotropy reduction given by the factor α is especially marked in the alloyed nanowires, where Pt promoted grain refinement. Then, in addition to the influence of crystallographic texture, Pt enhances the nanocrystalline nature of the NWs by promoting a large volume fraction of grain boundary-like lattice with crystallographic defects and non-negligible inter-grain exchange interaction. These factors are likely to reduce the magnitude of K_U in each NW. Small grains with sizes comparable to the exchange length in the alloy ($d_S \sim 2\ l_{ex} \sim 7$ nm, with $l_{ex} = \sqrt{\frac{2\ A}{\mu_0\ M_S^2}}$ the exchange length in the matrix, and A the Co exchange constant [29]) have a relatively large volume fraction of them exchange-coupled with neighboring grains (roughly given by $V_{exch} \sim \frac{3 l_{ex}}{d_S}$) leading to a reduction in K_U. The relatively square loops in CoPt55 with a definite critical reversal field are consistent with a quite strong inter-grain exchange interaction.

The coefficient α takes into account a reduction in anisotropy strength due to eventual inter-grain exchange coupling, non-isotropic easy axis orientation distributions and large areas of grain boundaries. A similar approach has been used in the past to describe the effective anisotropy field in nanocrystalline bulk hard magnets, with small grains partially coupled by exchange interaction [28]. In this model, a uniaxial anisotropy is also assumed and the magnetocrystalline anisotropy attenuation is accounted for by a coefficient α taking into account the regions of reduced K_U near grain boundaries, the effect of inter-grain exchange interaction and the relative disorientation between neighboring grains. Finally, these factors also contribute to lower K_U as compared with the constant K_U corresponding to the bulk phase.

In CoPt140 the grains are still small enough to introduce large grain boundary-like structures but they are somewhat larger, making the exchange interaction less efficient. Also, a higher porosity in this array increases demagnetizing interactions, therefore the magnetization reversal is governed by dipolar inter-wire interactions promoting an extended distribution of apparent critical fields, overcoming exchange effects. These two relevant interactions are further explored by performing a FORC analysis in both alloy arrays.

3.4 First Order Reversal Curves (FORC) analysis

Inter-nanowire dipolar and inter-grain exchange interactions are found to determine the experimental effective anisotropy in the arrays and the hysteresis parameters behavior as functions of the applied field orientation relative to the NW axis. Then, these interactions are further investigated for CoPt arrays with the same composition (CoPt55 and CoPt140) but with different porosity and grain size.

The FORC method is a powerful technique to analyze interactions in complex magnetic systems [30-33] and it has been successfully applied in numerous studies of NW [34-37]. FORC distributions can be especially effective and powerful in representing magnetization reversal processes in the case of highly interacting systems, approaching the problem from the elaboration of a physical model proposed by Béron *et al.* in 2008 [36] which is based on physically meaningful hypotheses.

To obtain the FORC distribution of a given magnet, several first order reversal curves must be measured, starting from an initially saturated state. From saturation, the applied field is decreased to a value H_r from which it is reversed and swept back to saturation. This procedure is repeated for different values of H_r and the magnetization $M(H_r, H)$ as a function of the applied field H is recorded at each step ($H_r \leq H$). From the $M(H_r, H)$ curves, the FORC distribution is calculated by taking the mixed derivative $\rho(H_r, H) = -\frac{1}{2}\frac{\partial^2 M(H_r\ H)}{\partial H_r\ \partial H}$. Contour plots of ρ are FORC diagrams. A clever approach to calculate $\rho(H_r\ , H)$ from the reversal curves $M(H_r, H)$ was given by A. Roberts et al. [38] who fitted the data points with a polynomial surface of the form $a_1 + a_2\ H_r + a_3\ H_r^2\ + a_4\ H + \ a_5 H^2\ + a_6 H_r\ H$ over a local grid which is centered at

each point. The value of $(-a_6)$ represents $\rho(H_r, H)$. In order to minimize noise amplification produced by the second derivative which defines $\rho(H_r, H)$, a smoothing factor SF is introduced. SF defines the size of the local fitting window, which contains $(2SF + 1)^2$ data points centered at each evaluation point. The FORC distribution is then given by $\rho(H_r, H) = -a_6$, where a_6 is obtained from the polynomial fit over this window. Increasing SF enlarges the fitting window, reducing noise contribution at the cost of spatial resolution. A common change of variables is usually done, from the (H_r, H) plane to the (h_c, h_u) plane, being $h_c = \frac{H - H_r}{2\mu_0}$ the coercive field axis and $h_u = \frac{H + H_r}{2\mu_0}$ the interaction field axis. The two parameters that characterize the FORC distributions are: the average coercive field, h_c^{FORC}, represented by the peak maximum, which can be taken as an estimate of the average coercive field of the individual NW [35,38,39]; and the interaction field distribution, Δh_u, which represents the maximum value of the interaction field (at saturation) [40].

Figure 5 and Figure 6 show the measured FORC distributions in the PA and PE field configurations for the two bimetallic samples.

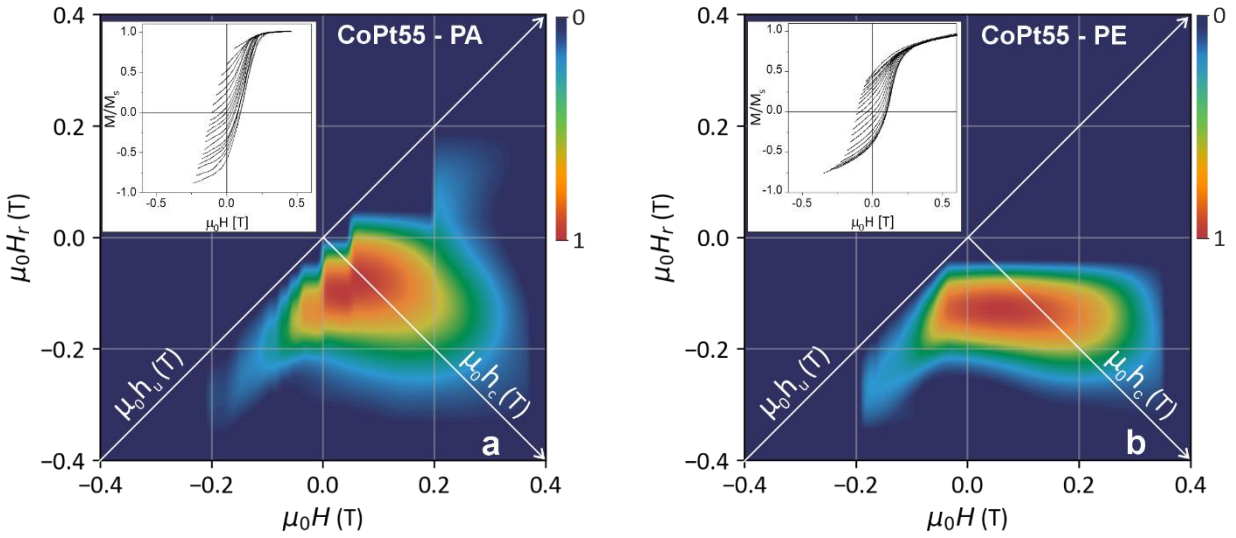

Figure 5. FORC diagrams corresponding to CoPt55 with the field applied along (a) the NW axis (PA configuration) and (b) perpendicular to this direction (PE). The insets display some of the curves measured for the analysis.

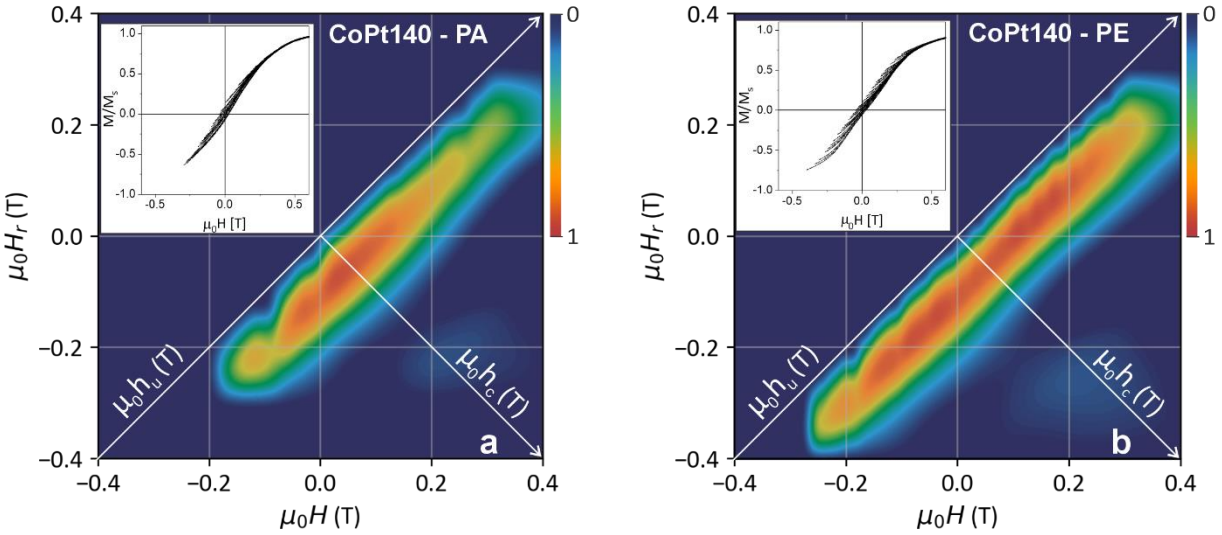

Figure 6. FORC diagrams corresponding to CoPt140 with the field applied along (a) the NW axis (PA configuration) and (b) perpendicular to this direction (PE). The insets display some of the curves measured for the analysis.

The values of the FORC parameters resulting from these data are summarized in Table 3. Each one of these quantities was determined by the conventional method explained in more detail in reference [41].

The FORC diagrams provide additional insight into the role of interactions in the magnetization reversal process. In CoPt55, the FORC distribution exhibits a characteristic "wishbone" shape, reflecting a broad distribution of switching fields combined with significant interaction effects [36,41-43]. Rather than indicating the presence of distinct magnetic phases, this feature is more consistently interpreted as arising from a heterogeneous anisotropy landscape with partially exchange-coupled regions.

While the wishbone-like FORC distribution is obtained for both applied field configurations (PA and PE), it may be observed that there is a marked shift of the h_c^{FORC} peak towards a higher value for the PA configuration and a lower value for the PE, confirming that the easy axis along $\varphi = 0$ is slightly preferred.

Table 3. Values of the reduced remanence m_r, the coercive field $\mu_0 H_c$ and the values of h_c^{FORC} and Δh_u for bimetallic samples CoPt55 and CoPt140, in both, PA and PE configurations.

		m_r	$\mu_0 H_c$	$\mu_0 h_c^{FORC}$	$\mu_0 \Delta h_u$
		[mT]	[mT]	[mT]	[mT]
CoPt55	PA	0.60	100	90	180
	PE	0.45	110	140	120
CoPt140	PA	0.16	60	80	490
	PE	0.13	62	70	600

Jafari *et al.* [43] observed that a wishbone distribution appears in samples presenting *two magnetic phases*-hard and soft. In our case, even when XRD results are consistent with a single crystalline phase in both bimetallic arrays investigated (a solid solution of Pt into *hcp* Co), the grain orientation distribution associated to crystalline texture and the small sized grains may induce a partially coupled ¨hard/soft magnetic phases" behavior, especially in CoPt55 (Figure 3b) where strongly exchange-coupled grains are expected.

In contrast, CoPt140 displays a pronounced spreading of the FORC distribution along the h_u axis (Figure 3c), indicative of strong magnetostatic interactions. This broadening reflects the distribution of effective interaction fields within the array, although it should not be interpreted as a direct measure of a single physical parameter. Instead, it results from the combined effects of mean interaction fields, local field variations, and correlations during reversal [36].

This feature coincides with what we see in both the major hysteresis loop and in the angle-dependent behavior of $\mu_0 H_c$ of this sample. In addition, we observe a larger value of Δh_u when the external field is applied in the plane of the array (PE configuration), thus requiring less energy to orient the magnetization along the axis of the NWs, a point that is not evident from the major loops alone. We also observe a slight dispersion along h_c for both configurations, with $h_c^{FORC} \approx H_c$ (see Table 3).

In summary, we observe that the FORC distributions in CoPt55 (the sample with the smallest grain size of ~10 nm) are consistent with exchange interactions between these grains and exhibit a characteristic wishbone shape, attributed to more than one magnetic contribution in the system; these two "magnetic phases" are likely the two families of *hcp* grains, with (100) and (110) orientations (both with the c-axis perpendicular to the NW axis) and grains oriented with the c-axis at 62º, that is, (101) orientation. On the other hand, FORC distributions for CoPt140 are consistent with high demagnetizing interactions both in PA and PE configuration. In this case, the larger porosity of the template together with larger grains (less exchange coupled) result in a FORC distribution characteristic of demagnetizing magnetostatic interactions.

4. Conclusion

The magnetic behavior of Co and Co-Pt nanowire arrays is governed by a complex interplay between crystallographic texture, grain size, exchange coupling, and dipolar interactions. The magnetocrystalline contribution to effective anisotropy in monophasic Co and $Co_{90}Pt_{10}$ NW arrays, exhibiting a strong crystallographic texture, is analyzed in the frame of the uniaxial anisotropy model.

The conventional uniaxial anisotropy model fails to describe Co-Pt nanowire arrays due to the breakdown of the assumption of a single effective magnetocrystalline anisotropy. In nanocrystalline systems with grain sizes comparable to the exchange length, inter-grain exchange coupling leads to a substantial reduction and averaging of the magnetocrystalline anisotropy. The relative importance of exchange and dipolar interactions can be tuned through microstructural parameters such as grain size and array porosity. These interaction regimes are clearly reflected in both angular-dependent hysteresis measurements and FORC diagrams.

Pt addition increases the texture strength as compared to that detected in pure Co, but reduces the NWs grain size. In CoPt55, as the grain size becomes comparable to twice the exchange length in the alloy, strong exchange inter-grain coupling inside the NWs are expected. This short-range interaction exchange-hardens the individual nanowires leading to more square hysteresis loops and higher coercivity and remanence. In CoPt140 this exchange interaction is less efficient to couple grains due to their larger size and the large contribution of dipolar interactions arising from a more porous template practically governs the array behavior.

FORC curves corresponding to the bimetallic arrays are consistent with highly interacting systems. In CoPt55, the distributions exhibit the *wishbone* or *boomerang* profile, typical of systems with two, partially coupled, magnetic phases. This profile is absent in CoPt140, where a broad distribution along the h_u axis is obtained, consistent with strong magnetostatic interactions.

Summarizing, the actual microstructure of each NW, in particular grain size and texture, become key parameters in modelling the magnetocrystalline energy contribution in polycrystalline nanowires.

These results highlight the need to incorporate microstructural effects explicitly when modeling the magnetic anisotropy of polycrystalline nanowires.

Conflict of Interest

The authors declare that they have no known competing financial interests or personal relationships that could have appeared to influence the work reported in this paper.

Acknowledgements

This work has been partially funded by Secyt-UNC, ANPCyT-FONCyT and Conicet (Argentina). The authors thank LAMARX-UNC for granting access to its SEM facility.

Data availability

The data that support the findings of this paper are available from the corresponding author, upon request.

References

[1] U. Santhi, W. K. Ngui, M. Samykano, K. Sudhakar, K. Kadirgama, B. Sangmesh, M. Asok Raj Kumar. Cobalt nanowires: Advancing into future nanomaterial, AIP Conf. Proc. 2059 (2019) 020006. https://doi.org/10.1063/1.5085949

[2] K. Gandha, K., Elkins, N. Poudyal, Liu Xubo, J. Ping Liu. High Energy Product Developed from Cobalt Nanowires. Sci Rep 4, 5345 (2014). https://doi.org/10.1038/srep05345.

[3] J. Mohapatra, M. Xing, J. Elkins, J. Beatty, J. Ping Liu. Extraordinary magnetic hardening in nanowire assemblies, Advanced Functional Materials 31(13) (2021) 2010157. https://doi.org/10.1002/adfm.202010157

[4] H. Zhu, J. Deng, Y. Yang, Y. Li, J. Shi, J. Zhao, Y. Deng, X. Chen, W. Yang. Cobalt nanowire-based multifunctional platform for targeted chemo-photothermal synergistic cancer therapy. Colloids and Surfaces B: Biointerfaces, 180 (2019)401-410. https://doi.org/10.1016/j.colsurfb.2019.05.005.

[5] A. Mukhtar, K. Wu, X. Cao, L. Gu. Magnetic nanowires in biomedical applications. Nanotechnology, 31(43) (2020) 433001Epub 2020 Jul 1. PMID: 32610303. https://doi.org/10.1088/1361-6528/aba1ba.
[6] S. Alotaibi, J. Samba, S. Pokharel, Lan Yucheng, K. Uradu, A. Afolabi, I. Unlu, G. Basnet, K. Aslan, B. N. Flanders, A. Lisfi, B. Ozturk. Individually grown cobalt nanowires as magnetic force microscopy probes, Appl. Phys. Lett. 112 (2018) 092401. https://doi.org/10.1063/1.4997310.
[7] L. Bu, S. Guo, X. Zhang, X. Shen, D. Su, G. Lu, X. Zhu, J Yao, J. Guo, X. Huang. Surface engineering of hierarchical platinum-cobalt nanowires for efficient electrocatalysis. Nat Commun 71 (2016) 1850. https://doi.org/10.1038/ncomms11850.
[8] W. Wang, X. Bai, X. Yuan, Y. Liu, L. Yang and F. Chang. Platinum-Cobalt Nanowires for Efficient Alcohol Oxidation Electrocatalysis Materials 16 (2) (2023) 840. https://doi.org/10.3390/ma16020840.
[9] S. Gupta, R. Fernandes, R. Patel, M. Spreitzer, N. D. Patel. A Review of Cobalt-based Catalysts for Sustainable Energy and Environmental Applications. Applied Catalysis A-General, 661 (2023) 119254. https://doi.org/10.1016/j.apcata.2023.119254
[10] Z. Liang, D. Shen, Wang, H. Fu. Recent progress of cobalt-based electrocatalysts for water splitting: Electron modulation, surface reconstitution, and applications. Nano Research, 17(4) (2024) 2234-2269. https://doi.org/10.1007/s12274-023-6219-4
[11] M. Shahid Arshad, SasˇoSˇturm, Janez Zavasˇnik, A. P. Espejo, J. Escrig, M. Komelj, P. J. McGuiness, S. Kobe, K.ˇZuzˇek Rozˇman. Effect of magnetocrystalline anisotropy on the magnetic properties of electrodeposited Co–Pt nanowires. J Nanopart Res 16 (2014) 2688. https://doi.org/10.1007/s11051-014-2688-4
[12] J. Zhang, G. A. Jones, T. H. Shen, S.E. Donnelly, G. Li. Monocrystalline hexagonal-close-packed and polycrystalline face-centered-cubic Co nanowire arrays fabricated by pulse dc electrodeposition. J Appl Phys 101 (2007) 054310– 054315. https://doi.org/10.1063/1.2464193
[13] H. Schlörb, V. Haehnel, M. S. Khatri, A. Srivastav, A. Kumar, L. Schultz, S. Fähler. Magnetic nanowires by electrodeposition within templates. Phys Status Solidi B 247 (2010) 2364–2379. https://doi.org/10.1002/pssb.201046189
[14] S. Yang, H. Zhu, D. Yu, Z. Jin, S. Tang, Y. Du. Preparation and magnetic property of Fe nanowire array. J Magn Magn Mater 222 (2000) 97–100. https://doi.org/10.1016/S0304-8853(00)00541-2
[15] N. Zafar, S. Shamaila, R. Sharif, H. Wali, S. Naseem, S. Riaz, M. Khaleeq-ur-Rahman. Effects of pH on the crystallographic structure and magnetic properties of electrodeposited cobalt nanowires. Journal of Magnetism and Magnetic Materials 377 (2015) 215–219 http://dx.doi.org/10.1016/j.jmmm.2014.10.105
[16] M. Darques, A. Encinas, L. Vila, L. Piraux. Controlled changes in the microstructure and magnetic anisotropy in arrays of electrodeposited Co nanowires induced by the solution pH. J. Phys. D: Appl. Phys. 37 (2004) 1411-1416. http://dx.doi.org/10.1088/0022-3727/37/10/001
[17] R. C. O'Handley. Modern Magnetic Materials: Principles and Applications. Wiley, 1999 ISBN: 0471155667, p 274.
[18] A. Kumar, S. Fähler, H. Schlörb, K. Leistner, L. Schultz. Competition between shape anisotropy and magnetoelastic anisotropy in Ni nanowires electrodeposited within alumina templates. Phys. Rev. B 73 (2006) 1-5. https://doi.org/10.1103/PhysRevB.73.064421
[19] J.D.L.T. Medina, G. Hamoir, Y. Velázquez-Galván, S. Pouget, H. Okuno, L. Vila, A. Encinas, L. Piraux. Large magnetic anisotropy enhancement in size controlled Ni nanowires electrodeposited into nanoporous alumina templates. Nanotechnology. 27 (2016) 145702. https://doi.org/10.1088/0957-4484/27/14/145702
[20] C. Bran, A.P. Espejo, E.M. Palmero, J. Escrig, M. Vázquez. Angular dependence of coercivity with temperature in Co-based nanowires, J. Magn. Magn. Mater. 396 (2015) 327–332. https://doi.org/10.1016/j.jmmm.2015.08.056
[21] F. Meneses, C. Bran, M. Vázquez, P. G. Bercoff. Enhanced in-plane magnetic anisotropy in thermally treated arrays of Co-Pt nanowires. Materials Science & Engineering B 261 (2020) 114669. https://doi.org/10.1016/j.mseb.2020.114669
[22] K. Nielsch, J. Choi, K. Schwirn, R. B. Wehrspohn, U. Gosele, Self-ordering regimes of porous alumina: the 10% porosity rule, Nano Lett. 2 (2002) 677-680
[23] [W. Lee, R. Ji, U. Gösele, K. Nielsch, "Fast fabrication of long-range ordered porous alumina membranes by hard anodization", Nature Materials 5, 9 (2006) 741.]
[24] G. B. Harris. Quantitative measurement of preferred orientation in rolled uranium bars. Philosophical Magazine 43 (1952) 113–123. https://doi.org/10.1080/14786440108520972

[25] A.L. Patterson, The Scherrer formula for X-ray particle size determination, Phys. Rev. 56 (1939) 978. http://dx.doi.org/10.1103/PhysRev.56.978
[26] F. Zighem, T. Maurer, F. Ott, G. Chaboussant. Dipolar interactions in arrays of ferromagnetic nanowires: A micromagnetic study. Journal of Applied Physics109(1) (2010) 1-8. https://doi.org/10.1063/1.3518498
[27] A. Aubert, K. Skokov, O. Gutfleisch. Journal of Magnetism and Magnetic Materials 634 (2025) 173566 https://doi.org/10.1016/j.jmmm.2025.173566
[28] H Kronmüller, K.-D. Durst, M. Sagawa Journal of Magnetism and Magnetic Materials 74 (1988) 291-302. https://doi.org/10.1016/0304-8853(88)90202-8
[29] R. C. O'Handley. Modern Magnetic Materials: Principles and Applications. ISBN: 978-0-471-15566-9- Page 192.
[30] M. I. Oliva, Paula G. Bercoff, Héctor R. Bertorello. First order reversal curves analysis of the temperature effect on magnetic interactions in barium ferrite with La–Co addition. Physica B: Condensed Matter 404 (2009) 2742-2745. http://dx.doi.org/10.1016/j.physb.2009.06.134.
[31] M.I. Oliva, H.R. Bertorello, P.G. Bercoff. Switching field of partially exchange-coupled particles. Physica B: Condensed Matter 354 (2004) 203-208. http://dx.doi.org/10.1016/j.physb.2004.09.067.
[32] P. G. Bercoff, M. I Oliva, H. R Bertorello. Magnetic interactions and Preisach distributions of nanostructured barium hexaferrite. Physica B: Condensed Matter 320 (2002) 291-293. http://dx.doi.org/10.1016/S0921-4526(02)00718-4.
[33] M.I. Oliva, P.G. Bercoff, H.R. Bertorello. Application of FORC distributions to the study of magnetic interactions in ferrites of composition Ba1-xLax-δFe12-xCoxO19. Journal of Magnetism and Magnetic Materials 320 (2008), e100-e103. http://dx.doi.org/10.1016/j.jmmm.2008.02.034.
[34] E. M. Palmero, Fanny Béron, Cristina Bran, Rafael P del Real and Manuel Vázquez. Magnetic interactions in compositionally modulated nanowire arrays. Nanotechnology 27 (2016), 435705. http://dx.doi.org/10.1088/0957-4484/27/43/435705.
[35] M. Ciureanu, F. Béron, P. Ciureanu, R. W. Cochrane, D. Ménard, A. Sklyuyev, A.Yelon. First Order Reversal Curves (FORC) Diagrams of Co Nanowire Arrays. Journal of Nanoscience and Nanotechnology 8 (2008) 5725-5732. http://dx.doi.org/10.1166/jnn.2008.228.
[36] F. Béron, L. Clime, M. Ciureanu, Ménard, R. W. Cochrane, A. Yelon, Magnetostatic Interactions and Coercivities of Ferromagnetic Soft Nanowires in Uniform Length Arrays. Journal of Nanoscience and Nanotechnology 8 (2008), 2944-2954. http://dx.doi.org/10.1166/jnn.2008.159
[37] F. Béron, L.-P. Carignan, D. Ménard, A. Yelon. Extracting individual properties from global behaviour: first-order reversal curve method applied to magnetic nanowire arrays. Electrodeposited nanowires and their applications (2010), 167-88. http://dx.doi.org/10.5772/39475
[38] A. Roberts, C. Pike, K. Verosub. First-order reversal curve diagrams: a new tool for characterizing the magnetic properties of natural samples. Journal of Geophysical Research 105, B12 (2000) 28461-28475. https://doi.org/10.1029/2000JB900326
[39] S. Alikhanzadeh-Arani, M. Almasi-Kashi, A. Ramazani. Magnetic characterization of FeCo nanowire arrays by first-order reversal curves. Current Applied Physics 13 (2013), 664-669. http://dx.doi.org/10.1016/j.cap.2012.10.014.
[40] D. M. Burn, E. Arac, D. Atkinson. Magnetization switching and domain-wall propagation behavior in edge-modulated ferromagnetic nanowire structures. Physical Review B 88 (2013) 104422. http://dx.doi.org/10.1103/PhysRevB.88.104422.
[41] E. M. Palmero, M. Méndez, S. González, C. Bran, V. Vega, M. Vázquez, V. M. Prida. Stepwise magnetization reversal of geometrically tuned in diameter Ni and FeCo bi-segmented nanowire arrays. Nano Research 12 (2019) 1547-1553. http://dx.doi.org/10.1007/s12274-019-2385-9.
[42] C. Dobrota, A. Stancu. "What does a first-order reversal curve diagram really mean? A study case: Array of ferromagnetic nanowires". Journal of Applied Physics 113 (2013), 043928. http://dx.doi.org/10.1063/1.4789613
[43] E. Jafari-Khamse, M. Almasi Kashi, A. Ramazani. Angular dependence of interactions in polycrystalline Co nanowire arrays. Materials Chemistry and Physics 159 (2015), 128-138. http://dx.doi.org/10.1016/j.matchemphys.2015.03.062.